

USING NUMERICAL MODELING TO DETERMINE VISCOUS LOSSES WITHIN  
HELIUM TURBOMACHINERY

by

BENJAMIN UHLIG

Presented to the Faculty of the Graduate School of  
The University of Texas at Arlington in Partial Fulfillment  
of the Requirements  
for the Degree of

MASTER OF SCIENCE IN AEROSPACE ENGINEERING

THE UNIVERSITY OF TEXAS AT ARLINGTON

December 2020

Copyright © by Benjamin Uhlig 2020

All Rights Reserved



## Acknowledgements

I would like to thank Dr. Frank Lu for all his support and for encouraging me to join this project and become part of the Aerodynamics Research Center team. I would also like to thank the other members of my committee: Dr. Donald Wilson and Dr. Ratan Kumar. Additionally, I would like to thank David Carter and Purushotham Balaji as well as the support teams at Pointwise®, NASA-FUN3D, and the Texas Advanced Computing Center for all their support dealing with all manner of technical issues which arose. Finally, I would like to thank my parents and my wife for their help and encouragement as I pursued higher education.

December 1, 2020

## Abstract

# USING NUMERICAL MODELING TO DETERMINE VISCOUS LOSSES WITHIN HELIUM TURBOMACHINERY

Benjamin Uhlig, MS

The University of Texas at Arlington, 2020

Supervising Professor: Frank Lu

As the consumption of energy has increased relentlessly over the last few decades, the need for reliable clean energy generation has increased as well. Currently, nuclear power is the only method capable of providing a stable supply of clean energy, although the nuclear energy generation process still requires improvement. Specifically, there is a need to increase efficiencies while reducing the risks of radioactive contamination. It is possible that both these issues may be mitigated using helium as the working fluid.

However, the performance of turbomachinery using helium must be evaluated before its use can be implemented. To do this, Balaji and Wilson [Analytical Modeling of Helium Compressor Performance," AIAA Paper 2016-4958, July 2016, <https://doi.org/10.2514/6.2016-4958>] developed a code, "HeComp", to estimate the performance of a helium compressor. In this code, the flow is treated as inviscid and analytic models are used to estimate the compressor pressure losses.

The present study utilized a Navier-Stokes solver, FUN3D, to predict the viscous pressure losses more accurately and compare the results to those of the "HeComp" code. The findings show that the pressure losses presented by the "HeComp" code are marginally larger than those calculated in this study.

## Table of Contents

Acknowledgements .....	iii
Abstract .....	iv
List of Illustrations .....	vi
List of Tables .....	vii
List of Symbols .....	viii
Chapter 1 : Introduction.....	9
Chapter 2 : Modeling Numeric Simulations.....	13
NACA 65-210 Farfield Mesh.....	13
Rotor Channel Mesh.....	19
Stator Channel Mesh.....	21
Chapter 3 : Results and Discussion.....	24
NACA 65-210 Farfield.....	24
Stator Channel.....	29
Chapter 4: Conclusions and Recommendations for Future Work .....	34
References.....	35

## List of Illustrations

Figure 1: NACA 65-210 Farfield Mesh.....	14
Figure 2: NACA 65-210 Boundary Region Near the Leading Edge .....	15
Figure 3: NACA 65-210 Initial Spacing Near the Leading Edge .....	16
Figure 4: NACA 65-210 Grid Independence – Lift Coefficient.....	17
Figure 5: NACA 65-210 Grid Independence - Drag Coefficient.....	17
Figure 6: Rotor Channel Mesh.....	19
Figure 7: Rotor Channel Single Block Mesh.....	20
Figure 8: Rotor Channel Multi-Block Structure .....	21
Figure 9: Stator Channel Mesh .....	22
Figure 10: Stator Channel Grid Independence .....	23
Figure 11: NACA 65-210 Residuals.....	25
Figure 12: NACA 65-210 Coefficients.....	25
Figure 13: NACA 65-210 Farfield Flowfield .....	26
Figure 14: NACA 65-210 Airfoil Flowfield .....	27
Figure 15: NACA 65-210 Leading Edge Flowfield .....	27
Figure 16: NACA 65-210 Results and Comparison .....	28
Figure 17: Stator Channel Residuals.....	30
Figure 18: Stator Channel Coefficients .....	30
Figure 19: Stator Channel Overall Flowfield .....	31
Figure 20: Stator Channel Leading Edge Flowfield .....	32
Figure 21: Stator Channel Boundary Layer Flowfield .....	32

## List of Tables

Table 1: NACA 65-210 Grid Convergence.....	18
Table 2: Stator Channel Grid Convergence.....	23
Table 3: NACA 65-210 Model Characteristics .....	24
Table 4: NACA 65-210 Results and Comparison .....	28
Table 5: Stator Channel Model Characteristics .....	29
Table 6: Stator Channel Results and Comparison .....	33

## List of Symbols

$AOA$	Angle of Attack
$\alpha$	Flow Angle
$C$	Chord Length
$d$	Stagger Angle
$e$	Error
$f_{1-4}$	Results of Each Grid Level
$f_{h=0}$	Estimation of True Value
$F_s$	Safety Factor
$GCI_{1-4}$	Grid Conversion Index of Each Grid Level
$\lambda$	Stagger Angle
$M$	Mach Number
$N$	Order of Convergence
$P$	Pressure
$r$	Refinement Ratio
$Re$	Reynolds Number
$T$	Temperature
$y^+$	Dimensionless Initial Wall Spacing

## Subscripts

01	Total Inlet Value
02	Total Outlet Value
1	Inlet Value
2	Outlet Value
$\infty$	Freestream Value



## Chapter 1 : Introduction

The consumption of energy globally has been steadily rising since the 1950's. Between 1970-2014, the average per capita energy consumption globally has increased by 45 percent [1]. As the demand for energy has grown, so has the need for efficient and reliable electricity production methods. The four leading methods by which electricity is produced worldwide are coal, gas, hydropower, and nuclear. Although oil is currently the most consumed energy source globally, its consumption is primarily from its use in transportation, and it therefore represents a significantly smaller percentage of electricity generation.

Generation of electricity from both coal and gas is accomplished by using these materials as fuel which is burned to produce heat. A major advantage of this method is the ability to adjust to daily demand and produce only the amount of electricity currently needed. Additionally, both methods have been in use since the 1800s, and have benefited from many years of research and development, resulting in efficiencies which can exceed 50 percent. However, neither of these methods are environmentally friendly due to the emissions created during the combustion process.

Hydroelectric electricity production has the greatest efficiency of any method currently in use, over 80 percent. These facilities employ turbines and generators to convert the kinetic energy carried by water as it flows downstream into electricity. In systems which contain a heating or combustion stage, a sizable percentage of energy is lost in the form of waste heat, leading to lower efficiencies. The absence of a heating or combustion stage within the hydroelectric process leads to significantly greater efficiencies. Since this process does not rely on combustion, it also does not produce emissions, making it the largest source of green energy worldwide. The primary constraints of hydroelectric facilities are the requirement for a suitable water source and the environmental impacts. The site must not only be able to provide enough flow for electricity generation but must also be capable of accepting the facility without having a negative impact on the ecosystem around it.

Nuclear power plants are currently the fourth largest producer of electricity worldwide. Like coal and gas facilities, nuclear power plants use fuel to generate heat and subsequently, electricity. However, unlike those facilities, nuclear power is not generated through combustion. Instead, a nuclear reactor houses fuel rods which are filled with small fuel pellets formed from fissionable material, such as uranium or plutonium. When these materials undergo nuclear fission, they produce heat, which is used to generate steam, which is then used to run a turbine. The turbine drives an electrical generator that converts the kinetic energy into useable electricity. Historically, a cooling tower then pumps cool water through a condenser, which converts the steam back into liquid. The water is then pumped into the steam generator, where it cools the reactor while being converted into steam, restarting the cycle. Since this process does not rely on combustion to produce electricity, it does not produce emissions and is therefore the second largest source of clean energy worldwide.

The common characteristic of the four electricity production methods listed above is their ability to produce energy consistently. Although the use of other renewable methods such as wind and solar have increased significantly over the last decade, they are severely limited by their dependence on environmental conditions. For example, solar energy can only be produced when the sun is shining. While the use of energy storage systems does have the potential to mitigate this issue, they are not advanced enough to provide a complete solution at this time. Therefore, to provide a consistent source of electricity, these methods must be supplemented with one of the four methods listed above.

Of those methods, coal and gas both produce greenhouse gas emissions and do not represent viable long-term solutions for the future. Similarly, hydroelectric power is limited by the number of locations which can support those facilities, and the ability to effectively transport that electricity to the location where it will be used. This restricts the areas which can be supported by hydroelectricity and keeps it from being a universal solution. This leaves nuclear energy as the ideal primary electricity source for the future.

While nuclear energy has many positive qualities, there are still many challenges which must be addressed. The cost of building a nuclear facility is currently greater than each of the other three methods, with it costing up to twice that of a coal facility and six times that of natural gas [2]. Nuclear power is also less efficient to produce than coal or gas when these methods use a combined-cycle process. Finally, nuclear power plants generate greater safety concerns from the public due to the radioactive material being used and the possibility of radioactive contamination. To mitigate the challenges associated with nuclear energy, research is currently being performed to improve the process by which electricity is generated within these power plants.

In 1945 Professor Ackeret, a co-founder of the closed Brayton cycle, suggested the use of a closed-cycle gas turbine power conversion system within the nuclear process [3]. This would convert the system from open-cycle and water-cooled to closed-cycle and gas-cooled. This concept had many potential benefits which included increased cycle efficiency and the ability to select the gas used to cool the system.

The use of helium as the working fluid within the closed-cycle cooling system provides several additional benefits [4]. The most significant of these are the increased heat transfer coefficient and the fact that helium is a non-radioactive inert gas. The increased heat transfer coefficient allows helium to absorb heat much more quickly than water, allowing it to be a more efficient coolant. As a non-radioactive inert gas, the use of helium in the closed cycle reduces the risk of radioactive contamination during the plant's operation to nearly zero, increasing safety factors while also reducing the wear on mechanical components.

Using helium within this system also presents challenges, with the largest being the increased cost of helium and the turbomachinery stages of the closed Brayton cycle. Helium has a specific heat which is approximately five times that of air. This means that any turbomachinery using helium as the working fluid must be designed specifically for this task. For example, helium passing through a single compressor stage will experience one-fifth the

pressure rise of what would occur when running air [5]. Therefore, helium compressors require many more stages to achieve the same pressure increase, when compared to air compressors.

When designing turbomachinery which uses helium as the working fluid, it is necessary to develop a means of predicting the performance of each component before testing. An analytical model “HeComp” has been developed for this purpose by Balaji [6]. Although this code produced results which were in good agreement with the results from experimental testing [7], further improvement was desired. One of the limitations of the code was its use of loss models, which were formulated using the cascade data of air compressors, due to the lack of helium compressor data.

The present study was conducted to improve these loss models by supplementing the available air compressor cascade data with data calculated using a computational fluid dynamics (CFD) solver. These CFD solvers have been used extensively in aerospace engineering and provide a reliable alternative when experimental testing is not desirable.

Due to the high Reynolds number exhibited by the flow, it was necessary to account for the effects of turbulence within the model. A Reynolds-averaged Navier-Stokes (RANS) turbulence model, the Spalart-Allmaras (SA) model, was implemented for this purpose. The SA model is a single-equation model developed for use with aerodynamic flows, which features both speed and robustness. It was acceptable for this application due to the lack of boundary layer separation or eddies within the flow.

## Chapter 2 : Modeling Numeric Simulations

The numerical simulations conducted in this study relied on the use of four software packages. Modeling of geometry as well as mesh generation were performed using Pointwise®. Three-dimensional meshes were required by the solver. Thus, two-dimensional structured meshes were created and extruded in a third dimension. This made it possible to run the meshes within the solver, while still being able to consider the results as two-dimensional. The next software used was NASA's Navier-Stokes solver, FUN3D. This solver utilizes node-based, finite-volume discretization to perform a wide array of CFD functions [8]. Finally, ParaView and VisIt were both used for post-processing and generating figures. A local desktop computer was used to complete all mesh generation and post processing, while FUN3D was run on the Texas Advanced Computing Center's (TACC) Lonestar 5 computing system.

### NACA 65-210 Farfield Mesh

The purpose of the NACA 65-210 farfield model, shown in Figure 1, was to allow a set of solutions from FUN3D to be compared to known experimental data. This was necessary to verify that the installation, setup, and execution of the FUN3D code was performed correctly. The mesh generated for this purpose consists of a NACA 65-210 airfoil with a chord length of 2 ft set at an angle of attack of  $2^\circ$ . The airfoil is contained within a farfield boundary which extends 10 times the airfoil chord length upstream, and 20 times this length downstream. This was done to avoid having the flow at the airfoil's leading edge affect the boundary conditions upstream and to properly capture the wake region downstream.

A distance scale is not included in any of the mesh figures shown in this study. This is because neither Pointwise nor FUN3D apply units to the models. Instead, a reference length is applied outside of these programs to convert the non-dimensional values the programs use into dimensional values. The airfoil's chord length was selected to act as the reference length for each model presented in this study.

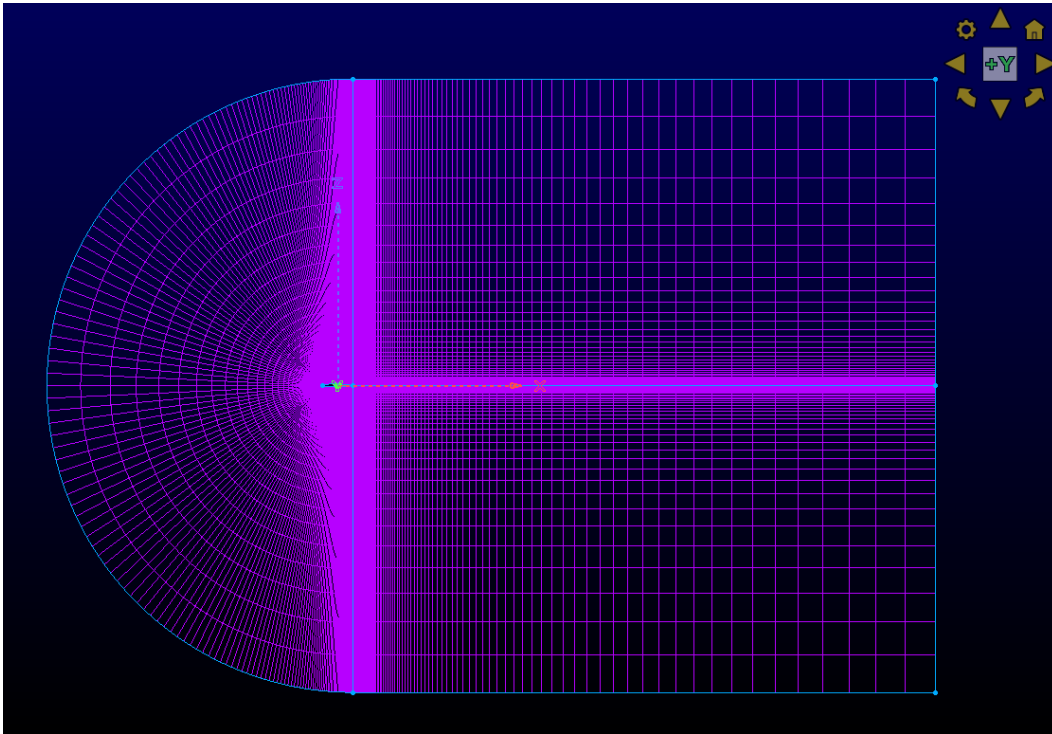


Figure 1: NACA 65-210 Farfield Mesh

A constant  $y^+ = 1$  was applied to all viscous surfaces present in this study (airfoils and compressor blades). The  $y^+$  values were determined using the Pointwise®  $y^+$  calculator. For this model, the initial spacing used to produce the required  $y^+$  was  $3.96 \times 10^{-6}$  m. The boundary layer region for this mesh is shown in Figure 2 and the initial spacing can be seen in Figure 3.

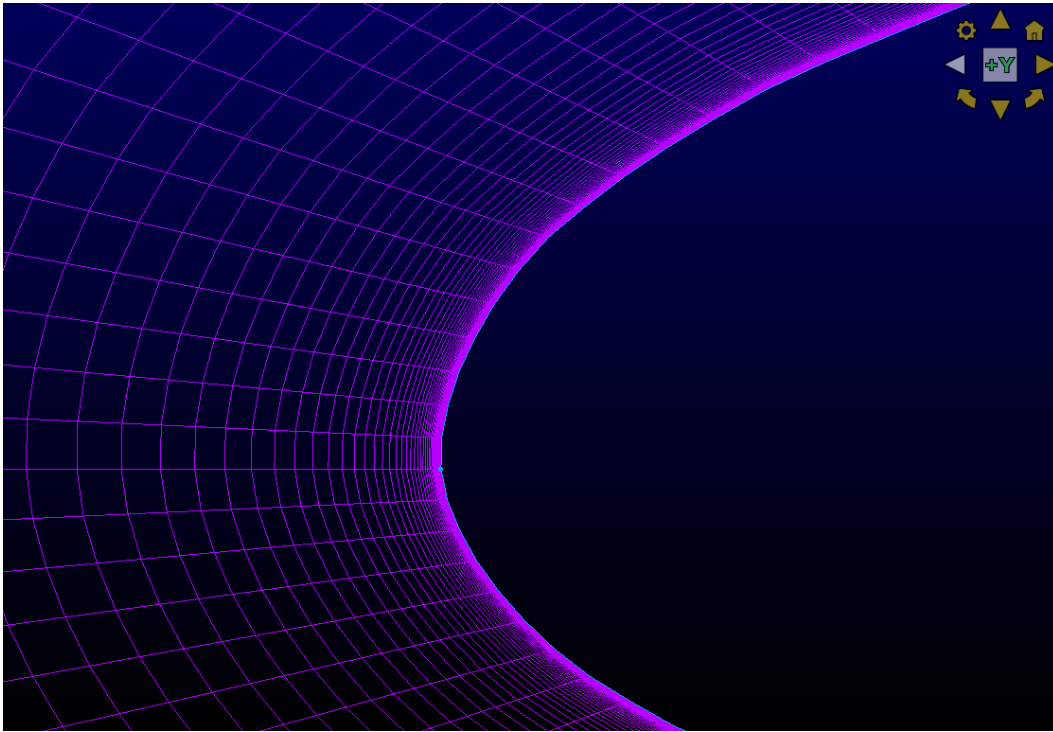


Figure 2: NACA 65-210 Boundary Region Near the Leading Edge

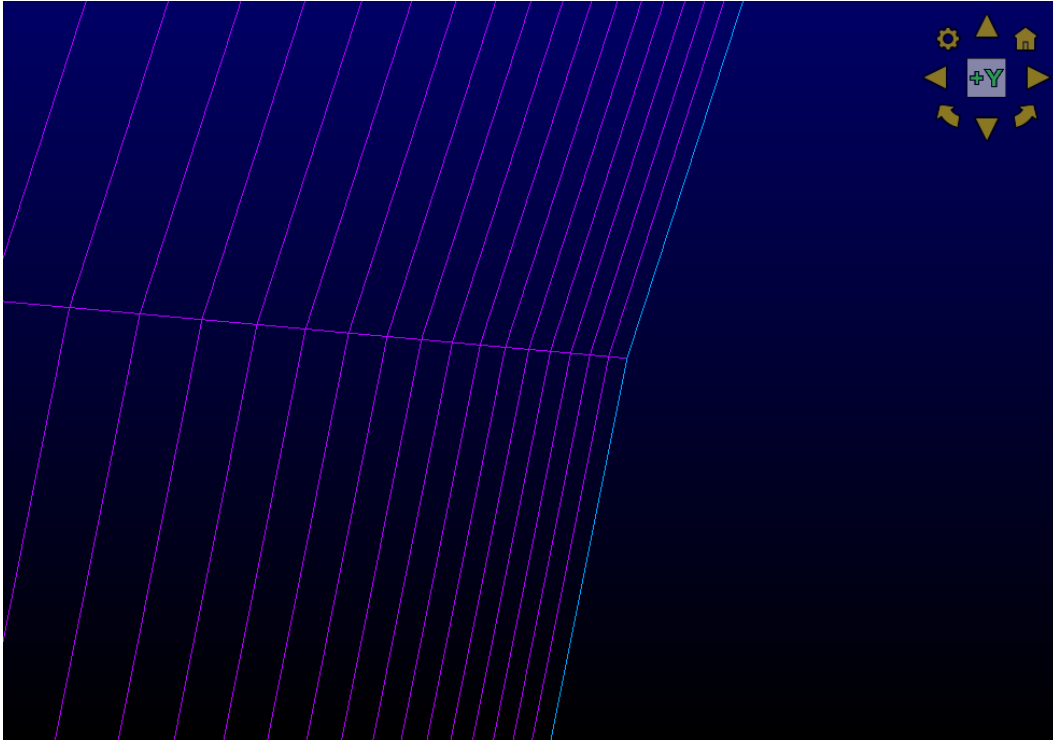


Figure 3: NACA 65-210 Initial Spacing Near the Leading Edge

To evaluate grid convergence, a set of four meshes were developed for each model used. These were produced by altering the mesh dimensions by a constant refinement ratio, resulting in fine (1), medium (2), coarse (3), and extra coarse (4) meshes. The model was then solved using each of the four meshes, tracking the effect on key parameters as well as the time required for the solver to complete the simulation. The result of this procedure on the NACA 65-210 model's lift and drag coefficients can be seen in Figures 4 and 5.





Figure 4: NACA 65-210 Grid Independence – Lift Coefficient

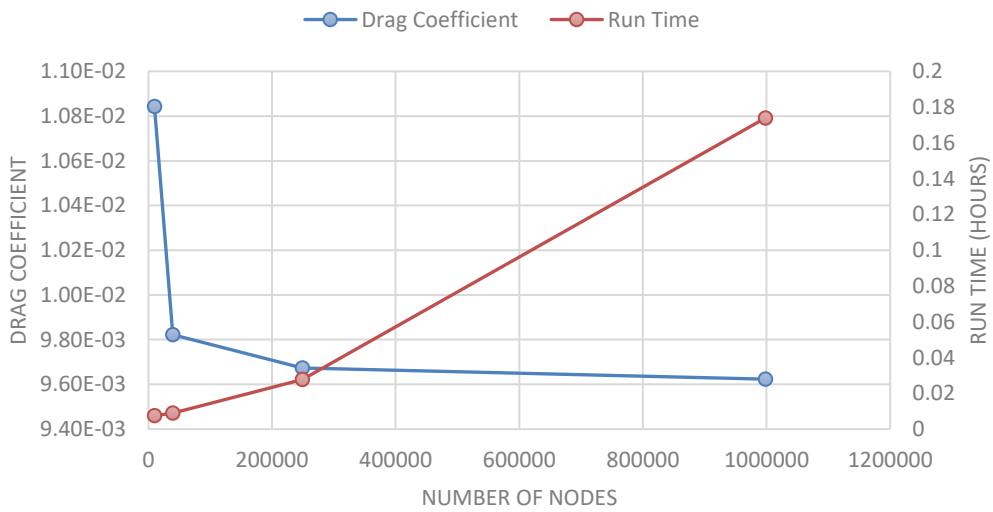


Figure 5: NACA 65-210 Grid Independence - Drag Coefficient

Using the results from the three finest meshes (1-3), several calculations were performed to evaluate grid convergence and results. The order of convergence was calculated using

$$N = \frac{\ln\left(\frac{f_3 - f_2}{f_2 - f_1}\right)}{\ln(r)} \quad [1]$$

A grid convergence index between mesh pairs was then determined using a factor of safety,  $F_S$ , of 1.25 and

$$GCI = \frac{F_S |e|}{r^N - 1} \quad [2]$$

Using the results from Equations [1] and [2], it was possible to check that the grid convergence was in the asymptotic range of convergence using

$$\frac{GCI_{2,3}}{r^N \times GCI_{1,2}} \cong 1 \quad [3]$$

Finally, an estimate of the true parameter values was determined based on the order of convergence and a Richardson extrapolation,

$$f_{h=0} = f_1 + \frac{f_1 - f_2}{r^N - 1} \quad [4]$$

The results of the above equations for both the lift and drag coefficient studies are provided in Table 1. Both parameters are shown to be within the asymptotic range of convergence. Therefore, the solution from the finest mesh (1) can be considered grid independent.

Table 1: NACA 65-210 Grid Convergence

Parameter	Symbol	Lift Coefficient	Drag Coefficient
Refinement Ratio	$r$	2.269	2.269
Order of Convergence	$N$	2.032	1.324
Grid Conversion Index	$GCI_{1,2}$	0.106	0.979
Grid Conversion Index	$GCI_{2,3}$	0.02	0.333
Asymptotic Range of Convergence		1.001	0.995
Richardson Extrapolation	$f_{h=0}$	$3.79 \times 10^{-1}$	$9.61 \times 10^{-3}$

## Rotor Channel Mesh

A single rotor blade was used to model the flow through the rotor channel. A blade centered topology was used instead of a passage centered topology. Using a blade centered topology, periodic boundaries are located half of the rotor stagger distance above and below the central blade. If a passage centered topology were used, these boundaries would occur at the leading and trailing edges and would intersect areas with high flow gradients, resulting in greater chances of solver instability. The inlet and outlet boundaries were offset 25 percent of the rotor chord length from the leading and trailing edges. An example of the rotor mesh can be seen in Figure 6.

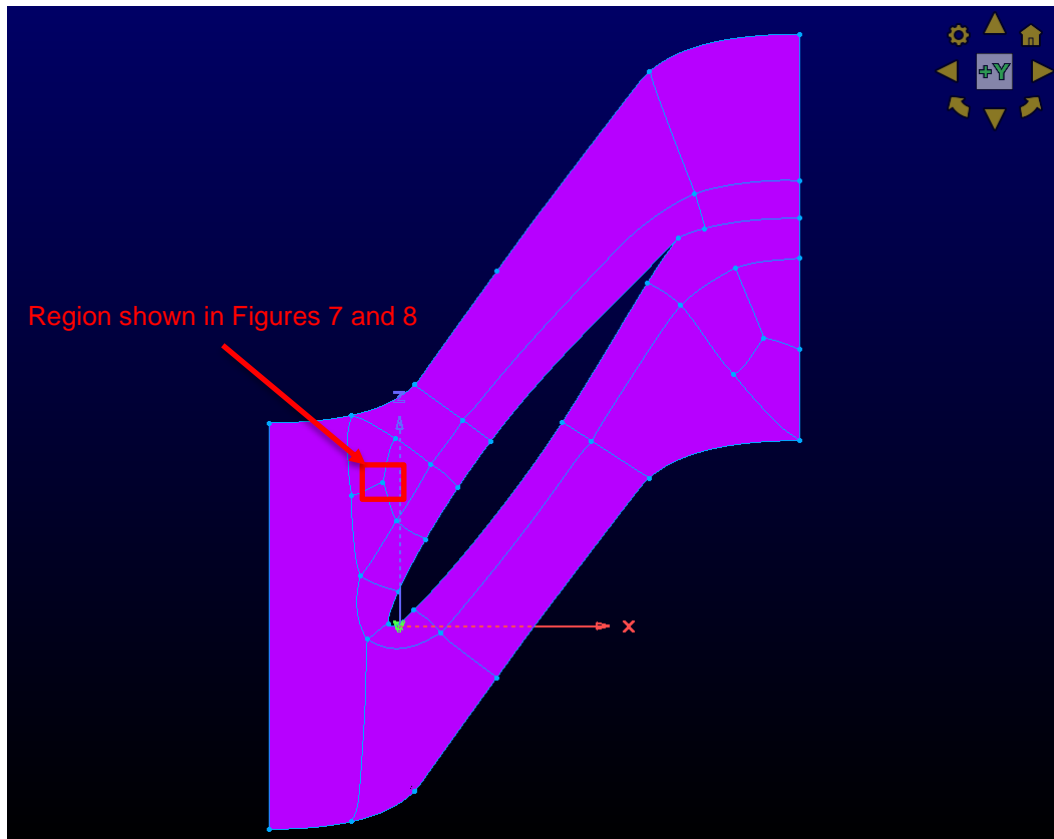


Figure 6: Rotor Channel Mesh

Due to the high stagger angle of the rotor, using a single structured block resulted in mesh cells being subject to large amounts of skewing, shown in Figure 7. This region in the computational domain is indicated in Figure 6.

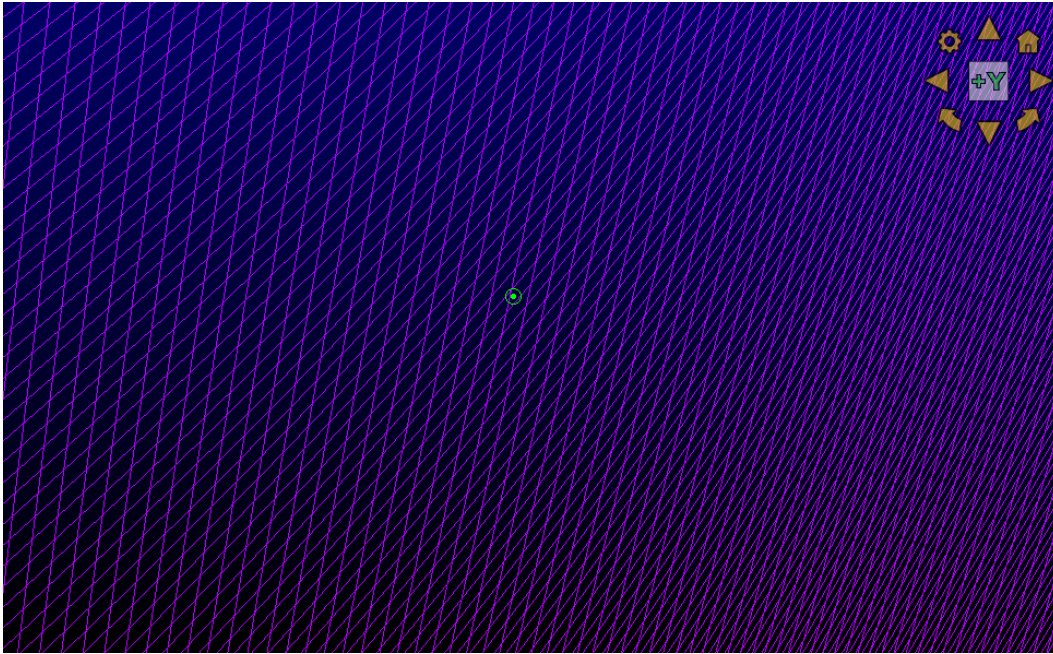


Figure 7: Rotor Channel Single Block Mesh

Therefore, it was necessary to divide the structured mesh into several smaller regions. An example of the high-quality meshing produced by these smaller blocks at the same location is shown in Figure 8, where the blue lines show the edges of the additional blocks.

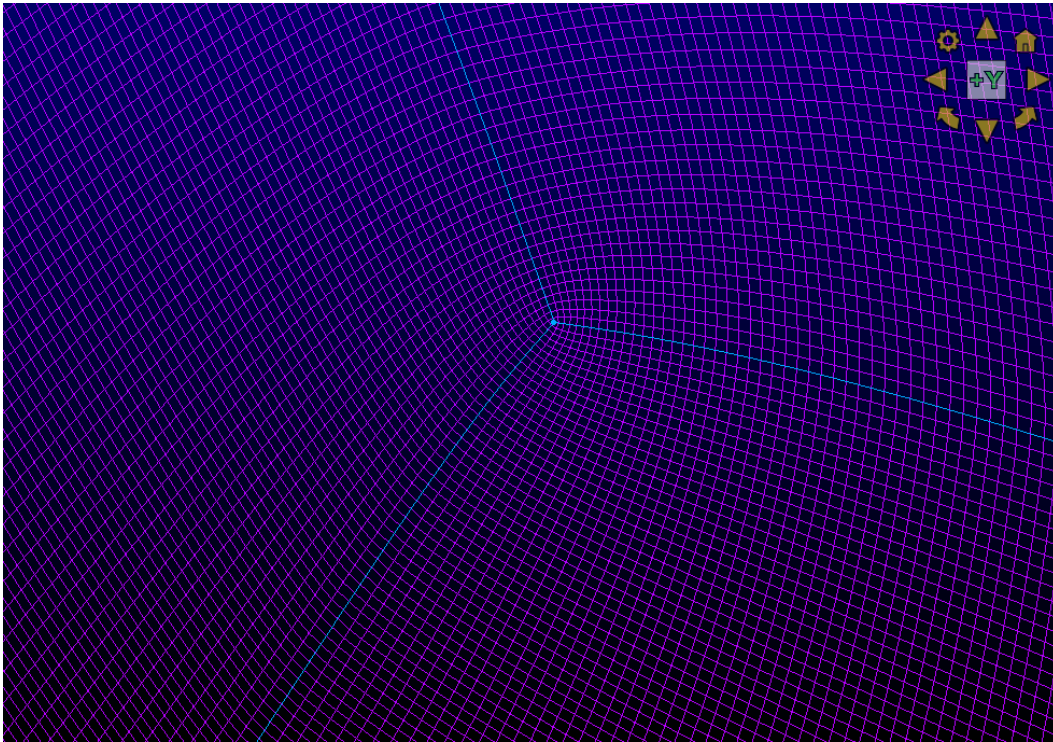


Figure 8: Rotor Channel Multi-Block Structure

Due to limitations of the inlet boundary condition, which was used to initialize the flow within FUN3D, inlet angles which matched design conditions could not be achieved for either of the compressor models. In the case of the rotor model, inlet angles above  $45^\circ$  were not possible, resulting in an inability to produce useful solutions for the rotor. For this reason, results from this model are not included in this study and a grid convergence test was not performed. The next release of FUN3D is expected to include a new inlet boundary condition which resolves these issues.

#### Stator Channel Mesh

A blade centered stator channel mesh was also generated. The periodic boundaries above and below the blade were implemented with the same methods used for the rotor channel. However, the inlet and outlet boundaries were extended further from the blade, shown in Figure 9. Doing so reduced the interaction between the turbulent region near the blade and

the boundaries, allowing FUN3D to reach a converged solution. The mesh style was also transitioned from the C-grid, as seen in Figure 6, to an O-grid. This was done to remove the overly fine grid in the wake region, which was causing oscillations in the final solutions. To meet the requirement for a constant  $y^+ = 1$ , an initial spacing of  $1.5 \times 10^{-6}$  m was used.

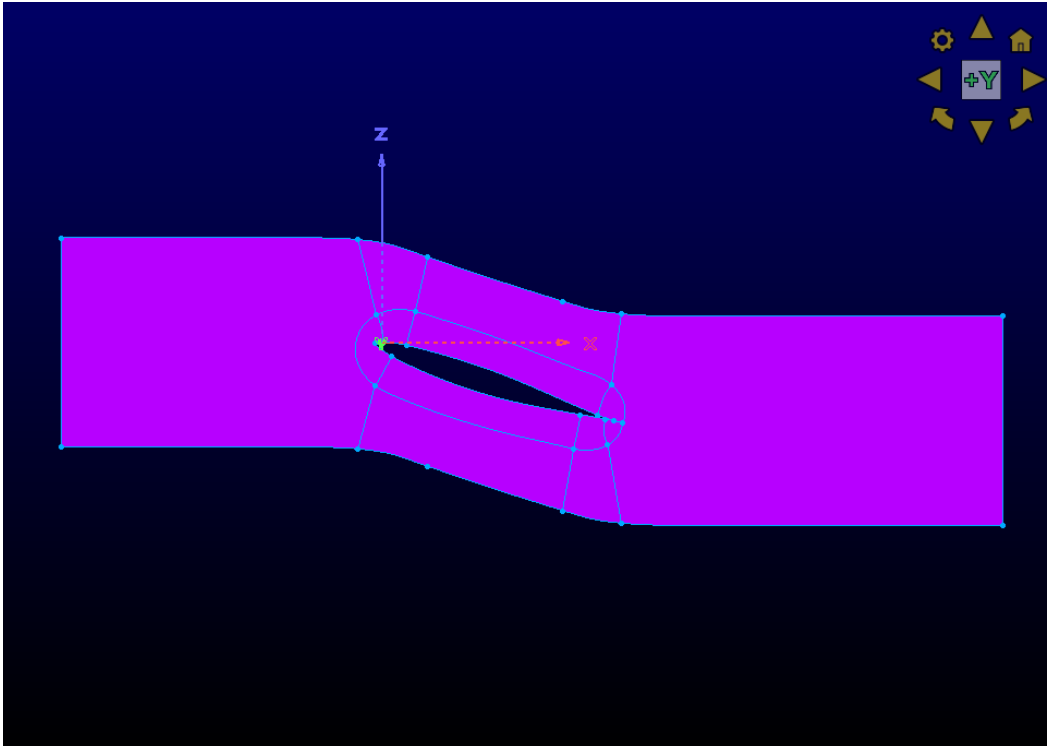


Figure 9: Stator Channel Mesh

Because the stagger and inlet angles were significantly lower for this model compared to the rotor model, it was possible to produce useful results, despite the difficulties presented by the inlet boundary condition. Therefore, a grid convergence study was performed using the same procedure followed for the NACA 65-210 model. The change in pressure loss and run time as the fineness of the mesh was increased can be seen in Figure 10.

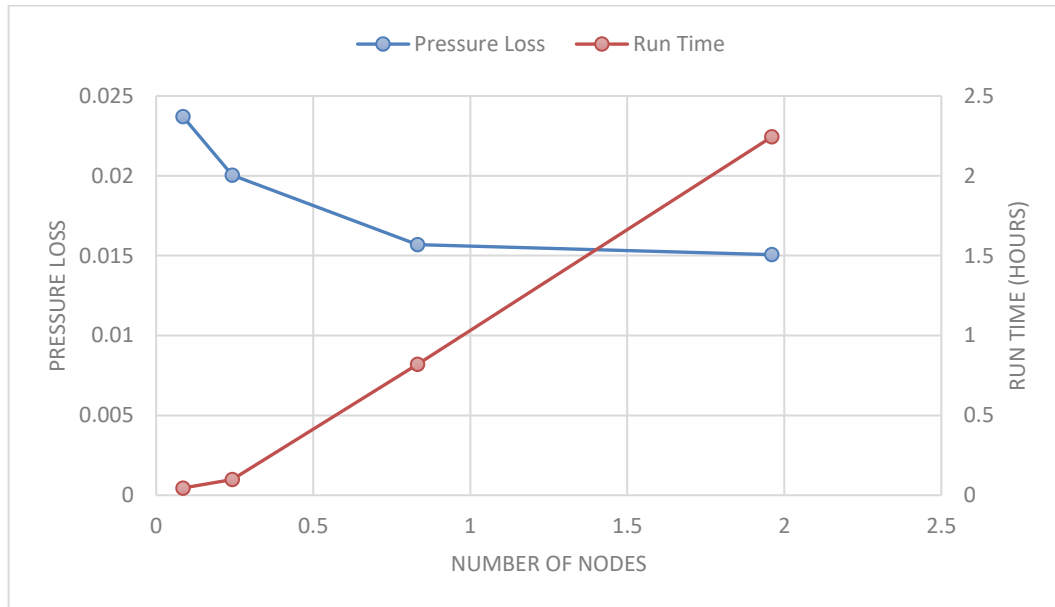


Figure 10: Stator Channel Grid Independence

As with the NACA 65-210 model, the results of the three finest stator meshes were then used within Equations [1-4] to quantify the convergence of the stator model. The resulting values, listed in Table 2, show that the solutions for the stator channel are within the asymptotic range of convergence. Therefore, the solution from the finest mesh (1) can be considered grid independent.

Table 2: Stator Channel Grid Convergence

Parameter	Symbol	Pressure Loss
Refinement Ratio	$r$	1.702
Order of Convergence	$N$	3.663
Grid Conversion Index	$GCI_{1,2}$	5.77
Grid Conversion Index	$GCI_{2,3}$	0.86
Asymptotic Range of Convergence		0.96
Richardson Extrapolation	$f_{h=0}$	$1.496 \times 10^{-2}$

## Chapter 3 : Results and Discussion

### NACA 65-210 Farfield

Before performing any simulations on the compressor models, it was necessary to validate the FUN3D installation and setup. This validation was completed by comparing known wind tunnel results to the results acquired from FUN3D when simulating the same experimental conditions. Since the NACA 65-210 airfoil was used in both the rotor and stator models, it was selected for use in the validation study as well. The wind tunnel experimental data was obtained from [9] for the NACA 65-210 airfoil with an angle of attack of 2°. The geometry and flow conditions used are listed in Table 3.

Table 3: NACA 65-210 Model Characteristics

<b>Parameter</b>	<b>Symbol</b>	<b>Value</b>	<b>Units</b>
Chord Length	$C$	2.0	ft
Angle of Attack	$AOA$	2.0	°
Reynolds Number	$R_e$	$3.00 \times 10^6$	Non-Dimensional
Freestream Mach Number	$M_\infty$	0.169	Non-Dimensional
Freestream Temperature	$T_\infty$	293.15	K

When evaluating the results from this simulation, and each subsequent simulation performed in this study, it was necessary to confirm that the simulation had reached a final and steady set of results. This was done by evaluating both the simulation's residuals, and the aerodynamic coefficient results. If each of the residuals had decreased by a factor of four, and there were no longer oscillations of more than 10% in the lift and drag coefficients, a model was considered to have converged. The results of this evaluation on the NACA 65-210 model can be seen in Figures 11 and 12.



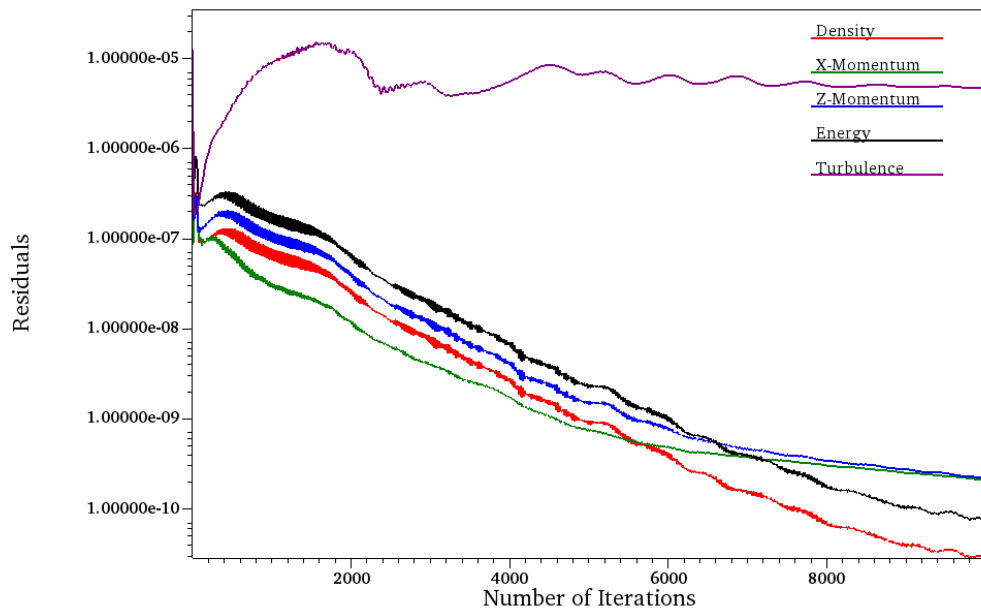


Figure 11: NACA 65-210 Residuals

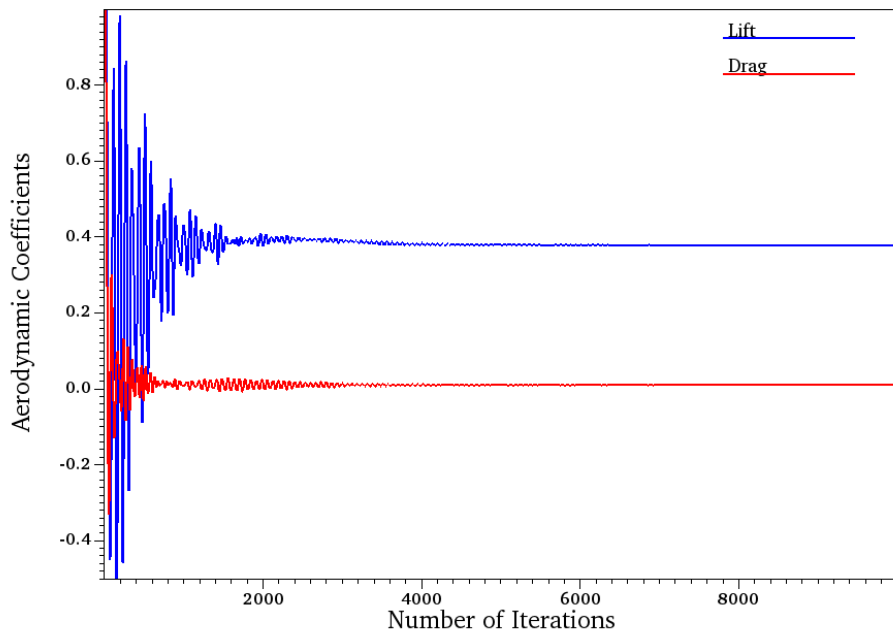


Figure 12: NACA 65-210 Aerodynamic Coefficients

The final step when checking for convergence was to view the simulation results within a two-dimensional flowfield. Visualizing the results in this manner was necessary to confirm that the flow did not have any unexpected behavior, such as reversed flow, which could be affecting the results. Figures 13-15 show the two-dimensional flowfield for the NACA 65-210 model from three unique viewpoints.

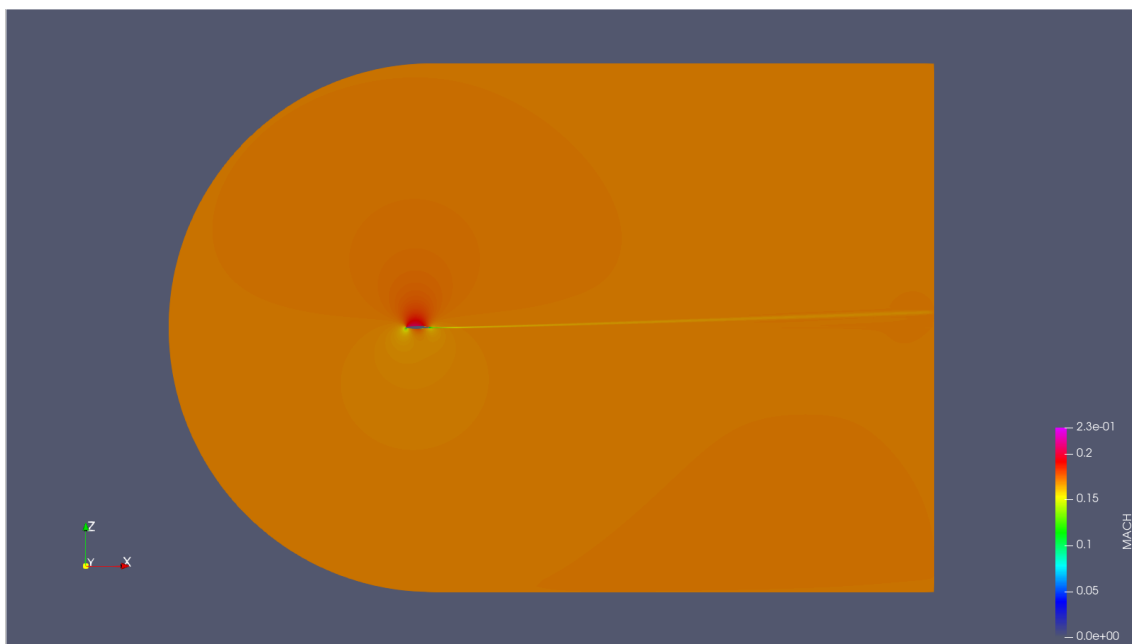


Figure 13: NACA 65-210 Farfield Flowfield

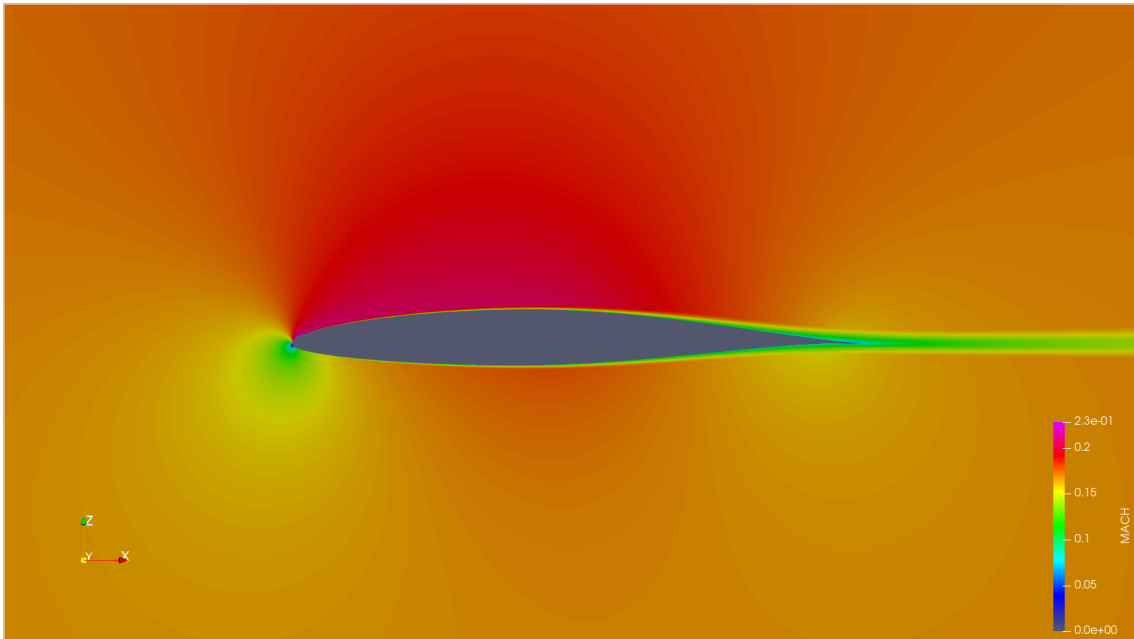


Figure 14: NACA 65-210 Airfoil Flowfield

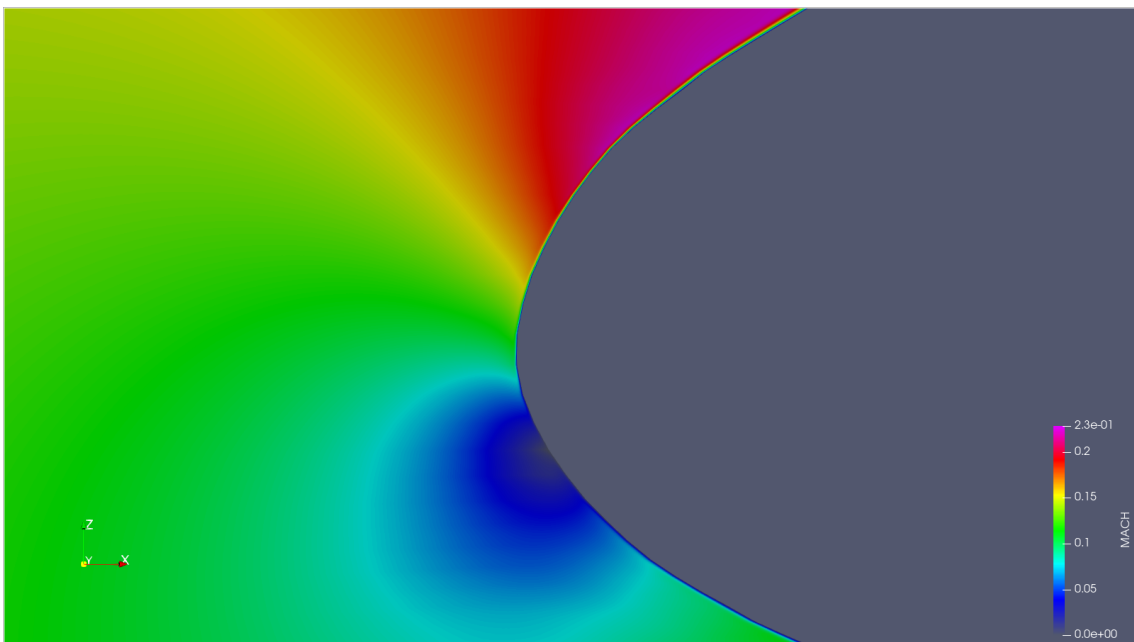


Figure 15: NACA 65-210 Leading Edge Flowfield

Figures 11 and 12 confirm that the convergence criteria have been met. Additionally, Figures 13-15 reveal no unexpected flow behaviors which would negatively affect the simulation results. Therefore, this simulation has converged.

Once convergence has been established, the results from the simulation could be compared to the known airfoil data. The values for each are listed in Table 4 and are plotted against each other in Figure 16.

Table 4: NACA 65-210 Results and Comparison

Parameter	FUN3D Simulation	Experimental Data
Coefficient of Lift	0.379	0.3 ↔ 0.4
Coefficient of Drag	$9.61 \times 10^{-3}$	$9.0 \times 10^{-3} \leftrightarrow 9.75 \times 10^{-3}$

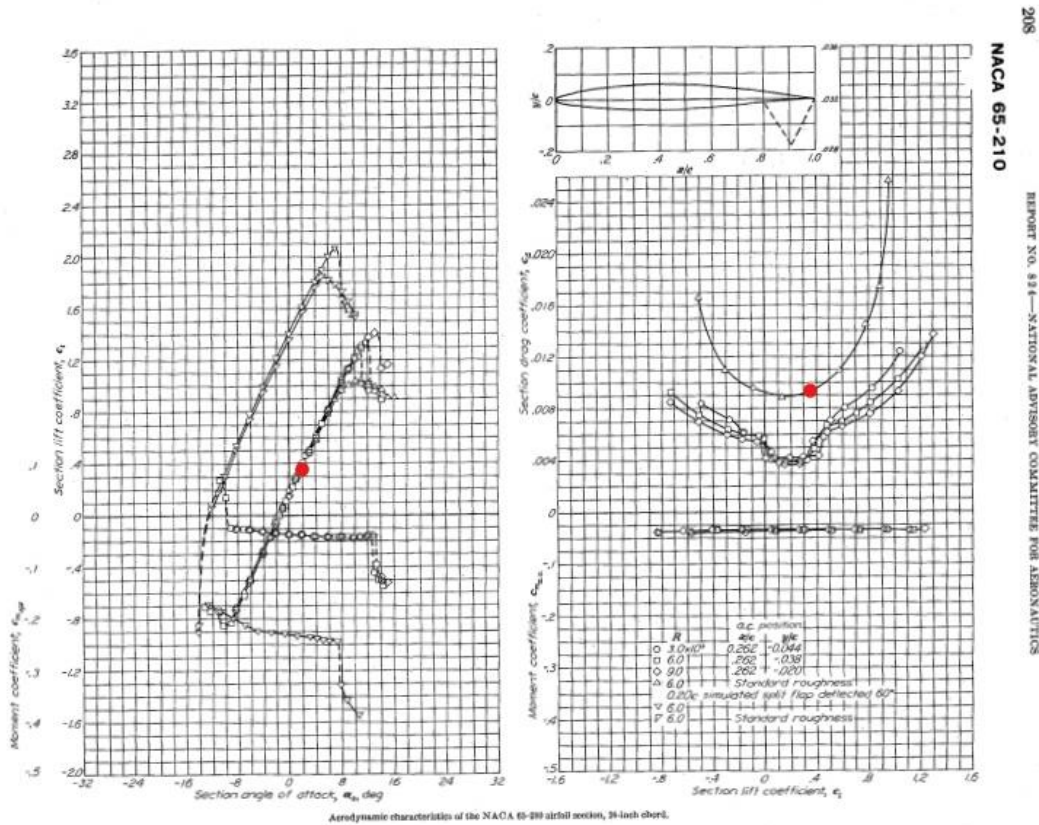


Figure 16: NACA 65-210 Results and Comparison

The results from FUN3D for both lift and drag coefficients are shown to be in good agreement with the experimental data. This confirms that the FUN3D installation and setup has been performed correctly and the compressor studies can begin.

#### Stator Channel

The primary purpose of this study was to evaluate the differences between the viscous pressure losses determined from the “HeComp” code and those calculated using FUN3D. Therefore, it was necessary to ensure that the geometry and flow conditions used for each of the two solvers was identical. Each of the values used for the stator channel model and “HeComp” code are listed in Table 5.

Table 5: Stator Channel Model Characteristics

<b>Parameter</b>	<b>Symbol</b>	<b>Value</b>	<b>Units</b>
Chord Length	$C$	$2.0 \times 10^{-2}$	m
Inlet Flow Angle	$\alpha_1$	33.5	°
Stagger Angle	$\lambda$	18.12	°
Stagger Distance	$d$	$1.66 \times 10^{-2}$	m
Reynolds Number	$R_e$	$2.85 \times 10^5$	Non-Dimensional
Inlet Mach Number	$M_1$	0.14	Non-Dimensional
Inlet Temperature	$T_1$	308.34	K

Once the FUN3D simulation was completed, it was necessary to evaluate the solution convergence using the same criteria listed for the NACA 65-210 model. Figure 17 shows the residuals having reduced by the required factor of four, and Figure 18 shows the absence of significant oscillations in the lift and drag coefficients.

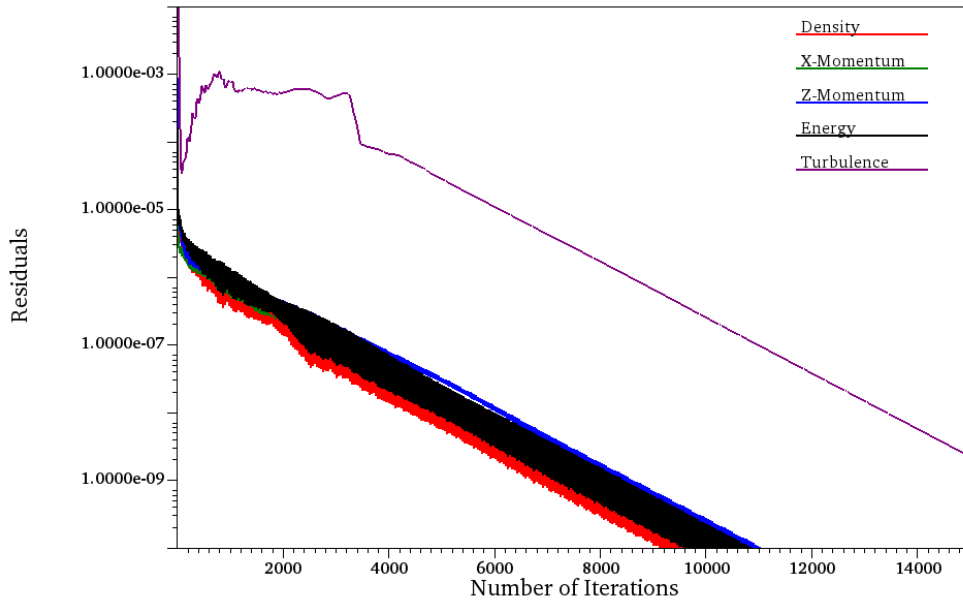


Figure 17: Stator Channel Residuals

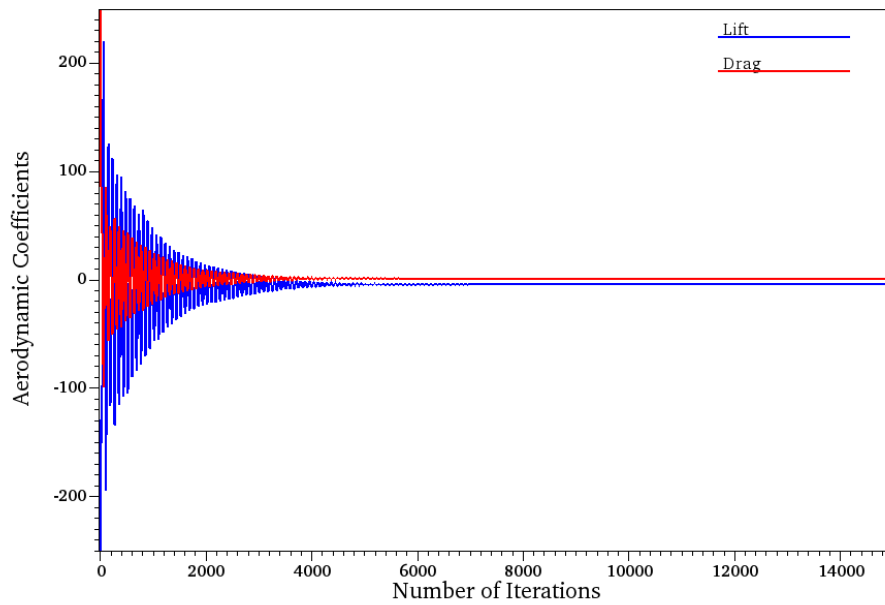


Figure 18: Stator Channel Aerodynamic Coefficients

As with the NACA 65-210 model, it is also necessary to view the two-dimensional flowfield for the stator to ensure that there is not any unexpected behavior affecting the results. Figures 19-21 show the stator channel's two-dimensional flowfield from a variety of viewpoints. As seen in these figures, no unwanted behavior has occurred within the flow that would cause inaccuracy in the final simulation results.

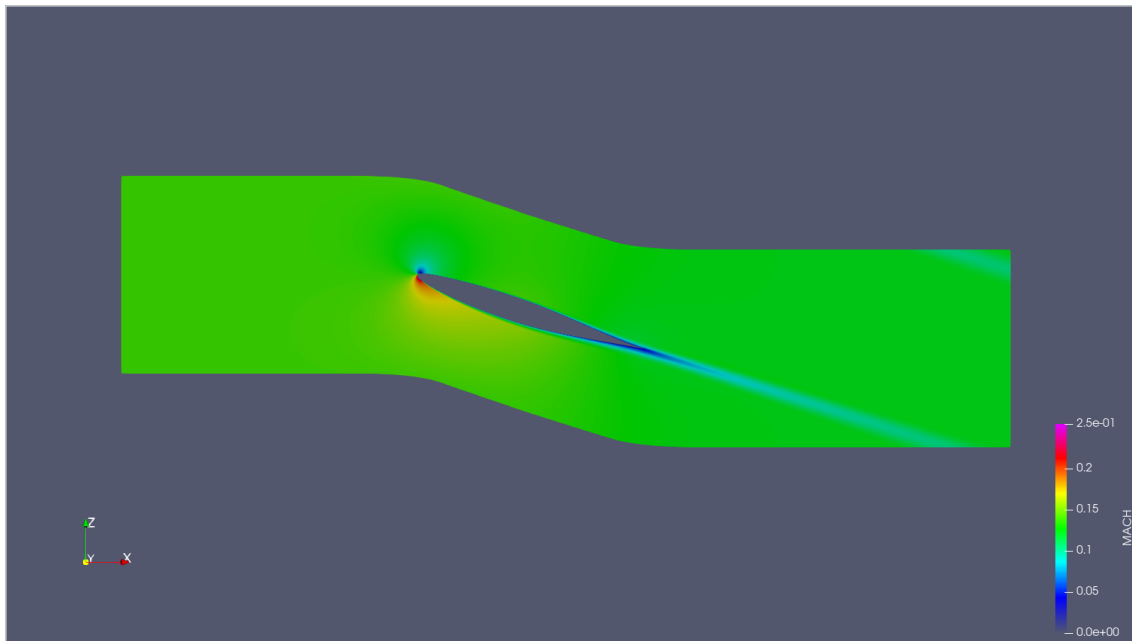


Figure 19: Stator Channel Overall Flowfield

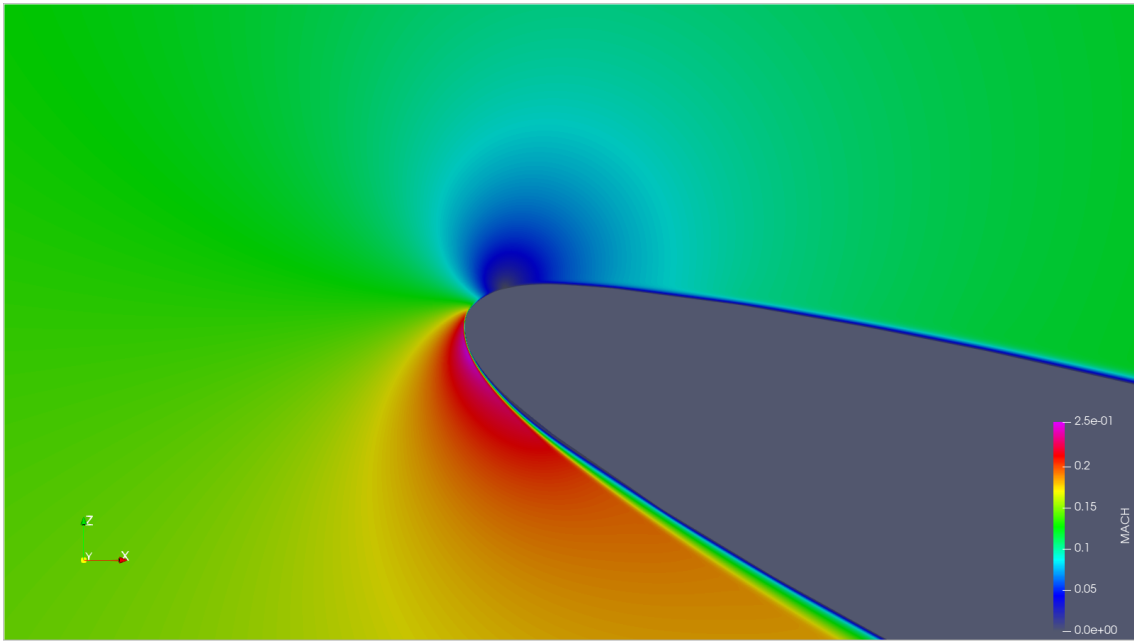


Figure 20: Stator Channel Leading Edge Flowfield

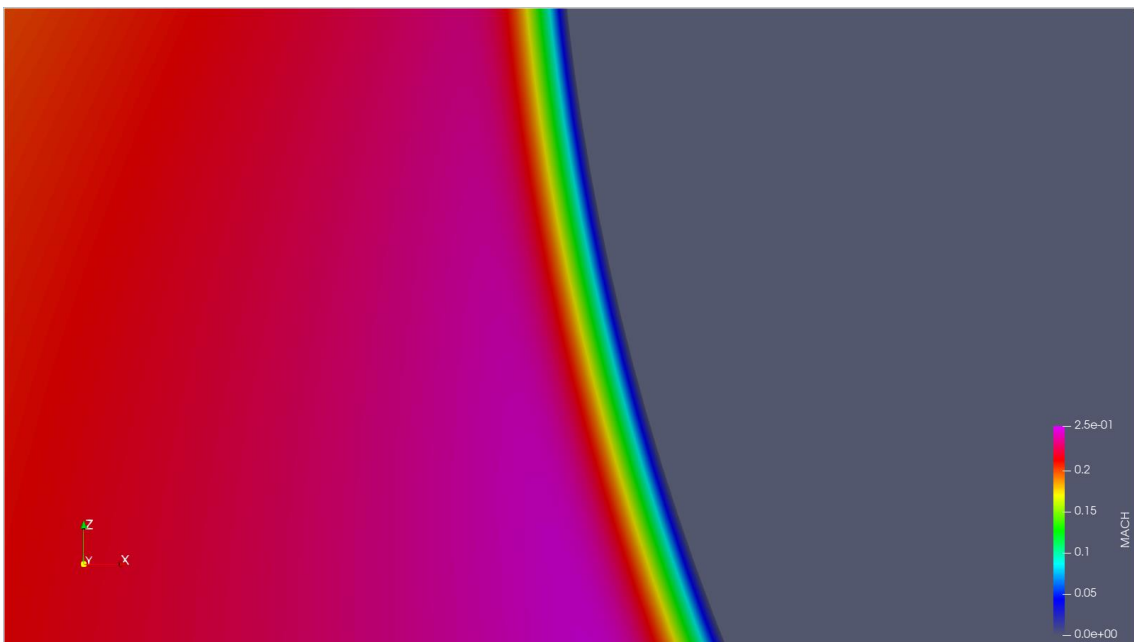


Figure 21: Stator Channel Boundary Layer Flowfield



It is clear from the residuals, coefficients, and flowfields shown above that the FUN3D simulation has converged. Therefore, it is possible to compare the FUN3D and “HeComp” code results. As previously stated, the parameter being compared is viscous pressure loss. The “HeComp” code includes this value in its list of outputs. However, it is not included in the outputs from the FUN3D simulation, so it was calculated from the other output parameters using,

$$P_{loss} = \frac{P_{01} - P_{02}}{P_{01} - P_1} \quad [5]$$

The values from viscous pressure losses determined from the “HeComp” code and the FUN3D simulation are shown in Table 6.

Table 6: Stator Channel Results and Comparison

Parameter	FUN3D Simulation	“HeComp” Code
Viscous Pressure Loss	$1.496 \times 10^{-2}$	$1.641 \times 10^{-2}$

The values listed above show the pressure loss determined from the “HeComp” code to be 9.24 percent larger than those calculated using the results from FUN3D. Part of this difference may be due to difficulties matching the inlet conditions between the two solvers, resulting in minor differences to the flow properties. However, the primary cause of the deviation comes from the differences in how each solver accounts for the effects of viscosity.

Unlike FUN3D, which utilizes a turbulence model and viscous terms to solve the turbulence equations, the “HeComp” code does not include viscous terms in the initial solution. Instead, it treats the flow as inviscid when solving, then applies loss models to estimate the effects of viscosity after the converged solution has been found. Since the loss models used in the “HeComp” code are meant to provide an estimate for the maximum viscous losses that may occur, it is expected that the values predicted using this solver are greater than those calculated using FUN3D, as seen in these results.

#### Chapter 4: Conclusions and Recommendations for Future Work

This study has shown that FUN3D can be used to accurately calculate the viscous pressure losses within a two-dimensional helium compressor stage. Unfortunately, the study was limited to evaluating the flow over the stator at a single set of flow angles. Although this made it impossible to improve the accuracy of the loss models used by the “HeComp” code, it did validate the results of those models by verifying that the predicted pressure losses were marginally larger than those calculated from the FUN3D simulation.

The next release of FUN3D is expected to resolve the inlet boundary condition issues faced in this study. If this is the case, it would be possible to conduct more simulations like those performed in this study and evaluate the performance of both the rotor and stator under a variety of flow conditions and blade angles. The results from those simulations could then be used to modify the “HeComp” loss models and improve the accuracy of the code’s performance predictions.

An alternative option for the continuation of this work would be to use a different simulation software, such as ANSYS Fluent. This would be beneficial as the FUN3D model used in this study was limited to two-dimensional flow and did not include rotation of the compressor blades. The use of a CFD program specifically designed for compressor simulations would allow flow conditions to be more finely controlled and the flow through the entire compressor to be evaluated

Regardless of which software is employed, it would be beneficial to begin performing high temperature turbine simulations as both helium compressors and turbines would be present in the closed-cycle nuclear cooling system.

## References

- [1] Ritchie, H., and Roser, M., "Energy," Our World in Data, retrieved 20 September 2020.  
<https://ourworldindata.org/energy>
- [2] "Capital Cost and Performance Characteristic Estimates for Utility Scale Electric Power Generating Technologies," Sargent & Lundy, SL-014940, Chicago, IL, December 2019.  
[https://www.eia.gov/analysis/studies/powerplants/capitalcost/pdf/capital\\_cost\\_AEO2020.pdf](https://www.eia.gov/analysis/studies/powerplants/capitalcost/pdf/capital_cost_AEO2020.pdf)
- [3] Mcdonald, C. F., "Helium Turbomachinery Operating Experience from Gas Turbine Power Plants and Test Facilities," *Applied Thermal Engineering*, Vol. 44, Mar. 2012, pp. 108–142.  
<https://doi.org/10.1016/j.applthermaleng.2012.02.041>
- [4] Guven, U., and Velidi, G., "Design of a Nuclear Power Plant with Gas Turbine Modular Helium Cooled Reactor," *Journal of Nuclear Engineering and Technology*, January 2011.  
[https://www.researchgate.net/publication/216315979\\_Design\\_of\\_a\\_Nuclear\\_Power\\_Plant\\_with\\_Gas\\_Turbine\\_Modular\\_Helium\\_Cooled\\_Reactor](https://www.researchgate.net/publication/216315979_Design_of_a_Nuclear_Power_Plant_with_Gas_Turbine_Modular_Helium_Cooled_Reactor)
- [5] Mattingly, J. D., Boyer, K. M., "Turbomachinery," *Elements of Propulsion: Gas Turbines and Rockets*, 2nd ed., AIAA, 2016.  
<https://doi.org/10.2514/4.103711>
- [6] Balaji, P., and Wilson, D. R., "Analytical Modeling of Helium Compressor Performance," AIAA Paper 2016-4958, July 2016.  
<https://doi.org/10.2514/6.2016-4958>
- [7] Yan, X., Takizuka, T., Kunitomi, K., Itaka, H., and Takahashi, K., "Aerodynamic Design, Model Test, and CFD Analysis for a Multistage Axial Helium Compressor," *Journal of Turbomachinery*, Vol. 130, No. 3, July 2008.

<https://doi.org/10.1115/1.2777190>

[8] Biedron, R. T., Carlson, J.-R., Derlaga, J. M., Gnoffo, P. A., Hammond, D. P., Jones, W. T., Kleb, B., Lee-Rausch, E. M., Nielsen, E. J., Park, M. A., Rumsey, C. L., Thomas, J. L., and Wood, W. A., "FUN3D Manual: 13.2", NASA Paper TM-2017-219661, August 2017.

[https://fun3d.larc.nasa.gov/papers/FUN3D\\_Manual-13.2.pdf](https://fun3d.larc.nasa.gov/papers/FUN3D_Manual-13.2.pdf)

[9] Abbott, I. H., and Von Doenhoff, A. E., Theory of Wing Sections: Including a Summary of Airfoil Data, New York: Dover, 2015.

<https://store.doverpublications.com/0486605868.html>

### Biographical Information

Benjamin Uhlig earned his bachelor's degree in Mechanical Engineering from Washington State University in 2017. His undergraduate studies included the completion of a senior design project. For this project, the undergraduate team worked for the Painted Dog Research Trust to fabricate an unmanned aerial vehicle which would be used to track African wild dogs in Zimbabwe. This project was his first significant exposure to the field of aerospace engineering and led him to enroll in the graduate program in aerospace engineering at The University of Texas at Arlington. Here he joined the Aerodynamics Research Center, where his research focused on computational fluid dynamics simulations of helium turbomachinery. He plans to continue working in this field after graduation.